Journal of
*Nuclear Engineering*

MDPI

*Article*

# Thermal Shock and Synergistic Plasma and Heat Load Testing of Powder Injection Molding Tungsten-Based Alloys

**Mauricio Gago [1,*], Steffen Antusch [2], Alexander Klein [2], Arkadi Kreter [1], Christian Linsmeier [1], Michael Rieth [2], Bernhard Unterberg [1] and Marius Wirtz [1]**

[1] Forschungszentrum Jülich, Institute of Fusion Energy and Nuclear Waste Management—Plasma Physics (IFN-1), 52425 Jülich, Germany; a.kreter@fz-juelich.de (A.K.); ch.linsmeier@fz-juelich.de (C.L.); b.unterberg@fz-juelich.de (B.U.); m.wirtz@fz-juelich.de (M.W.)
[2] Institute for Applied Materials, Karlsruhe Institute of Technology, 76344 Karlsruhe, Germany; steffen.antusch@kit.edu (S.A.); a.klein@kit.edu (A.K.); michael.rieth@kit.edu (M.R.)
* Correspondence: m.gago@fz-juelich.de

**Abstract**

Powder injection molding (PIM) has been used to produce nearly net-shaped samples of tungsten-based alloys. These alloys have been previously shown to have favorable characteristics when compared with standard ITER-grade tungsten. Six different alloys were produced with this method: W-1TiC, W-2$Y_2O_3$, W-3Re-1TiC, W-3Re-2$Y_2O_3$, W-1HfC and W-1$La_2O_3$-1TiC. These were tested alongside ITER-grade tungsten in the PSI-2 linear plasma device under ITER-relevant plasma and heat loads to assess their suitability for use in a fusion reactor. All materials showed good behavior when exposed to the lower pulse number tests ($\leq$1000 ELM-like pulses), although standard tungsten performed slightly better, with no observable difference in surface roughness. High-power shots, namely one laser pulse of 1.6 GWm$^{-2}$, revealed that samples containing yttria are more prone to melting and droplet ejection. After high pulse number tests (10,000 and 100,000 pulses), with and without plasma, the reference tungsten showed the most cracking and highest surface roughness of all materials, while the PIM samples seemed to have a higher resistance to cracking. This can be attributed to the higher ductility of these alloys, particularly those containing rhenium. This means that tungsten-based alloys, whether produced via PIM or other methods, could potentially be used in certain areas of a fusion reactor.

**Keywords:** nuclear fusion; tungsten; powder injection molding; PIM; plasma; PSI-2; ELM; thermal shocks; plasma-facing materials; divertor



Academic Editor: Dan Gabriel Cacuci

Received: 12 May 2025
Revised: 23 June 2025
Accepted: 4 July 2025
Published: 7 July 2025

**Citation:** Gago, M.; Antusch, S.; Klein, A.; Kreter, A.; Linsmeier, C.; Rieth, M.; Unterberg, B.; Wirtz, M. Thermal Shock and Synergistic Plasma and Heat Load Testing of Powder Injection Molding Tungsten-Based Alloys. *J. Nucl. Eng.* **2025**, *6*, 25. https://doi.org/10.3390/jne6030025



## 1. Introduction

Plasma-facing materials (PFMs) inside fusion devices are exposed to extreme particle and heat loads. During full DT operation ($Q_{DT}$ = 10), PFMs in the ITER divertor and possibly in DEMO are expected to withstand a stationary heat load of up to 10 MWm$^{-2}$ and a slow transient for several seconds of up to 20 MWm$^{-2}$ [1–4]. Additionally, PFMs will need to endure transient heat loads due to edge-localized modes (ELMs) which are expected to reach up to 1 GWm$^{-2}$ and have a duration of approximately 0.5 ms. Over $10^6$ such transient events are expected during the ITER divertor lifetime [3,5,6]. Moreover, divertor PFMs will face particle loads from plasma ions with a fluence to the order of $10^{26}$ m$^{-2}$ per pulse and $10^{30}$–$10^{31}$ m$^{-2}$ during their planned lifetime. Fusion neutrons will also cause damage to the material, which will amount to about 0.5 displacements per atom (dpa) [7].

Tungsten has been chosen as the plasma-facing material (PFM) for the ITER divertor due to its favorable material properties, such as a high melting point, low tritium retention, high thermal conductivity and low erosion rate (high energy threshold for sputtering) [2,8,9]. This makes it vital to test tungsten PFMs under the conditions under which they will operate in the ITER divertor. Previous tests have shown that tungsten mock-ups are able to withstand the stationary heat loads expected but carry the risk of producing macrocracks after exposure to a few hundred cycles of slow transient events of 20 $MWm^{-2}$ [10]. Additionally, ELM-like transient heat loads have been shown to cause surface damage, cracking, roughness, melting and recrystallization on tungsten samples [6,11]. Since, in a reactor, heat and plasma loads will impact PFMs simultaneously, the synergistic effects of both loads have also been investigated. These effects include the formation of tungsten fuzz, embrittlement of the material, increased cracking, bubble formation and localized melting [12–20].

The damage suffered by tungsten under the previously mentioned conditions indicates that PFMs could suffer catastrophic damage during the expected conditions in the ITER divertor and in future reactors such as DEMO. An example of the possible issues was observed in the EAST tokamak, where some tungsten divertor tiles have cracked and detached [21]. This makes developing new materials, particularly tungsten alloys that can better sustain such harsh conditions, of the utmost importance for the future of fusion energy. Tungsten-based alloys have been shown to have improved mechanical properties. The addition of rhenium, which forms a solid solution with tungsten, has shown improved ductility and toughness [22,23]. Solution softening seems to play a role in this case, increasing the dislocation density and bolstering deformation in the {1,1,2} slip plane [24–26]. Furthermore, finely dispersed grains of high melting point carbides and oxides, such as TiC, HfC, $Y_2O_3$ or $La_2O_3$, have also shown improved ductility and strength, increased resistance to recrystallization and grain growth and a lowering of the ductile-to-brittle transition temperature (DBTT) [26–32]. These carbides can disperse into the grain boundaries, hindering the grain boundary dispersion at high temperatures and strengthening them. Oxide phases can mitigate grain growth in recrystallized tungsten [33].

Powder injection molding (PIM) is a process that allows different materials, including materials with high melting points such as tungsten, to be mass produced with high performance, complex geometries and good mechanical properties [34–36]. This makes PIM an ideal method for developing tungsten alloys for use in fusion reactor divertors. PIM tungsten alloy samples produced at the Karlsruhe Institute of Technology (KIT) have been produced previously and tested at Forschungszentrum Jülich (FZJ), producing, in general, comparable results to those of ITER-grade reference tungsten [37]. Now, new PIM alloys have been produced and tested under fusion-relevant plasma and heat loads to test their viability as a PFM in the divertor of fusion reactors.

## 2. Materials and Methods

The used tungsten powder (>99.97 wt.% W) was mixed with a small quantity of a polymer (binder). The finished granulated so-called feedstock was used for injection molding of green parts. After shaping the green parts, the binder was extracted. The final sintering at temperatures above 2000 °C led to a density higher than 98%. Figure 1 shows the different steps in the production of W-PIM.

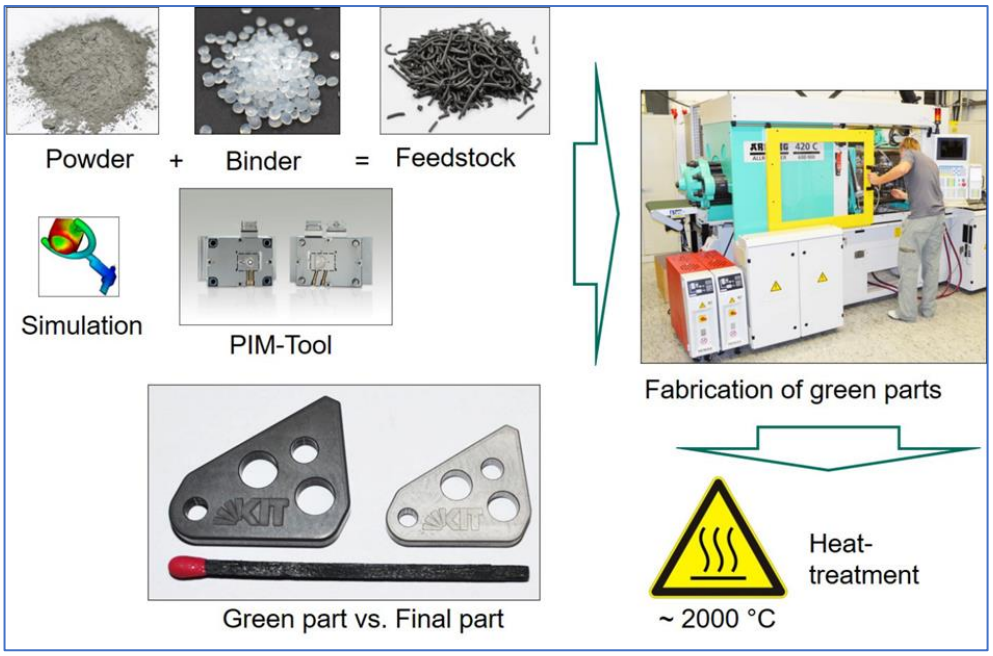


**Figure 1.** The main process's steps in W-PIM [32].

The fabrication of semi-finished parts (blocks or plates) via W-PIM and the subsequent mechanical machining is time- and cost-intensive. The solution was the design, development and fabrication of a new cavity to produce the samples via W-PIM (see Figure 2) for the PSI-2 linear plasma device at FZJ. The geometry and final shape of the samples can be seen in Figure 3.

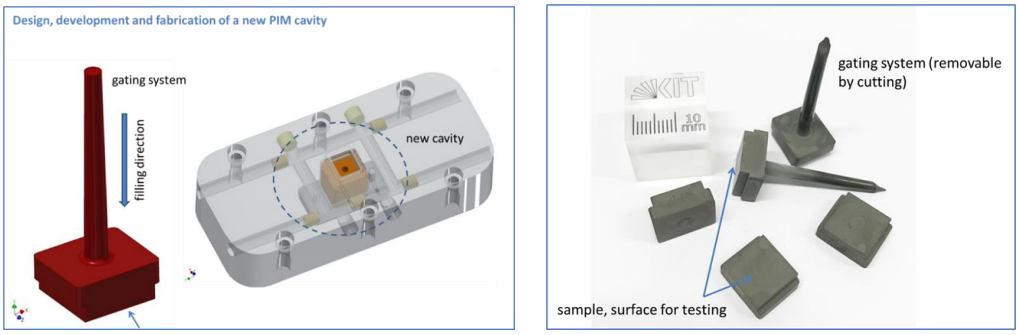


(**a**) (**b**)

**Figure 2.** (**a**) The design of the new cavity for the PIM tool. (**b**) Successful running-in of the new W-PIM cavity and fabrication of the first green-parts.

Six different tungsten-based alloys were produced with the PIM method at the KIT, whose microstructure and mechanical properties have been previously studied [32,35,36]. The tungsten-based alloys studied in this work are (by weight percent) W-1TiC, W-2$Y_2O_3$, W-3Re-1TiC, W-3Re-2$Y_2O_3$, W-1HfC and W-1$La_2O_3$-1TiC. Reference tungsten samples made of ITER-grade tungsten (ref. W) produced by PLANSEE in Austria were tested under the same conditions. Samples of each material with a geometry adapted for use in the PSI-2 linear plasma generator were produced. The samples had a thickness of 5 mm, with a top surface of 10 × 10 $mm^{-2}$ and a bottom surface of 10 × 12 $mm^{-2}$ and a 1 mm step on two sides. All samples were polished to a mirror finish, with a mean arithmetical roughness ($R_a$) of less than 0.1 µm. The samples were then tested in the PSI-2 under the conditions shown in Table 1 [38]. Testing conditions were designated as low pulse number testing

(LP), high pulse number testing (HP), and simultaneous plasma and high pulse number testing (PHP).

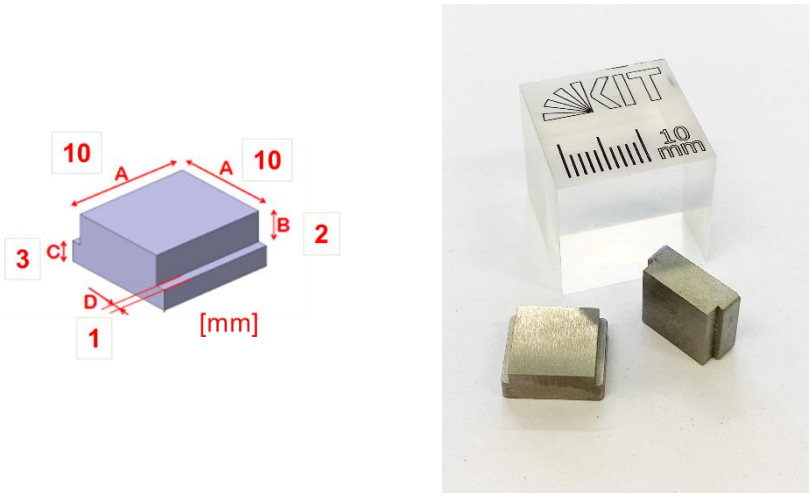


(**a**) (**b**)

**Figure 3.** (**a**) Geometry and (**b**) final shape of the W-PIM samples produced at the KIT.

**Table 1.** Testing conditions for the PIM-W and reference samples.

| Testing Condition | Base Temp. (°C) | Power Density ($GWm^{-2}$) | Heat Flux Factor $F_{HF}$ ($MWm^{-2}s^{-1/2}$) | Pulses | Plasma Flux ($m^{-2}s^{-1}$) |
|---|---|---|---|---|---|
| $LP_{1\text{-}400/1000}$ | 400/1000 | 0.19 | 6 | 100 | - |
| $LP_{2\text{-}400/1000}$ | | 0.38 | 12 | 100 | - |
| $LP_{3\text{-}400/1000}$ | | 0.38 | 12 | 1000 | - |
| $LP_{4\text{-}400/1000}$ | | 1.6 | 72 | 1 | - |
| $HP_{1\text{-}700}$ | 700 | 0.4 | 9 | $10^4$ | - |
| $HP_{2\text{-}700}$ | | 0.4 | 9 | $10^5$ | - |
| $PHP_{400/1000}$ | 400/1000 | 0.4 | 9 | $10^5$ | $3.6–4.4 \times 10^{21}$ |

These testing conditions were designed to simulate different fusion-relevant heat loads a PFM could be exposed to during its lifetime, particularly due to ELMs, and they have been used for testing similar materials in the past [11,13,37]. Plasma and heat load tests are designed to show the possible synergistic effects materials will undergo when exposed to both plasma and heat loads [12–14]. The different temperatures the materials were tested at show how the exposed PFMs could behave at different operational temperatures both below and above the DBTT of the reference tungsten.

In order to test the behavior and resistance of materials to thermal shocks by simulating the ELMs in a nuclear reactor, a pulsed Nd:YAG laser was used in PSI-2, with a wavelength of 1064 nm, a square profile and a produced laser spot about 3 mm in diameter. Low-pulse number tests (1–1000 pulses) were performed using 1 ms pulses (2 ms for the single high-power pulse) and a pulse frequency of 0.5 Hz, and high pulse number tests ($10^4$ and $10^5$ pulses) were performed using 0.5 ms pulses with a 10 Hz frequency.

Tests which simulated the synergistic effects of simultaneous heat and plasma loads were then performed [12,13]. The plasma was generated in the PSI-2 by an arc discharge using a $LaB_6$ cathode and then focused toward the sample with an axial magnetic field. A deuterium plasma with 6% helium was generated to simulate the plasma mix inside a fusion reactor [39]. Plasma fluxes of $3.6–4.4 \times 10^{21}$ $m^{-2}s^{-1}$ were generated, with an

incident ion energy of about 35 eV and a total plasma fluence of roughly $5 \times 10^{25}$ $m^{-2}$. The heat loads were produced simultaneously by the previously mentioned Nd:YAG laser.

## 3. Results and Discussion

After testing, all samples were analyzed with a laser profilometer to determine the change in their surface roughness as a measure of the surface modification and damage caused by the thermal shocks and plasma. The mean surface roughness ($R_a$) of each sample after testing under each condition is shown in Table 2 and in Figure 4.

**Table 2.** Summary of the mean surface roughness ($R_a$) of every material tested under every condition. $R_a$ is given in µm.

| Testing Condition | W-1TiC | W-2$Y_2O_3$ | W-3Re-1TiC | W-3Re-2$Y_2O_3$ | W-1HfC | W-1$La_2O_3$-1TiC | Ref. W |
|---|---|---|---|---|---|---|---|
| **$LP_{1\text{-}400}$** | 0.09 | 0.26 | 0.12 | 0.12 | 0.13 | 0.12 | 0.10 |
| **$LP_{2\text{-}400}$** | 0.11 | 0.28 | 0.13 | 0.13 | 0.15 | 0.14 | 0.09 |
| **$LP_{3\text{-}400}$** | 0.30 | 0.37 | 0.22 | 0.19 | 0.34 | 0.36 | 0.11 |
| **$LP_{4\text{-}400}$** | 0.89 | 3.17 | 0.81 | 5.67 | 0.87 | 0.96 | 0.18 |
| **$LP_{1\text{-}1000}$** | 0.10 | 0.07 | 0.19 | 0.13 | 0.14 | 0.12 | 0.10 |
| **$LP_{2\text{-}1000}$** | 0.14 | 0.25 | 0.20 | 0.18 | 0.19 | 0.16 | 0.11 |
| **$LP_{3\text{-}1000}$** | 0.38 | 0.52 | 0.33 | 0.47 | 0.43 | 0.31 | 0.39 |
| **$LP_{4\text{-}1000}$** | 0.74 | 4.91 | 0.81 | 5.99 | 1.31 | 0.86 | 0.24 |
| **$HP_{1\text{-}700}$** | 0.48 | 0.46 | 0.43 | 0.45 | 0.73 | 0.57 | 0.66 |
| **$HP_{2\text{-}700}$** | 0.49 | 0.56 | 0.45 | 0.51 | 0.91 | 0.59 | 16.2 |
| **$PHP_{400}$** | 0.45 | 2.88 | 0.44 | 0.48 | 0.50 | 0.45 | 2.70 |
| **$PHP_{1000}$** | 1.26 | 1.37 | 0.44 | 0.50 | 2.19 | 1.07 | 4.49 |

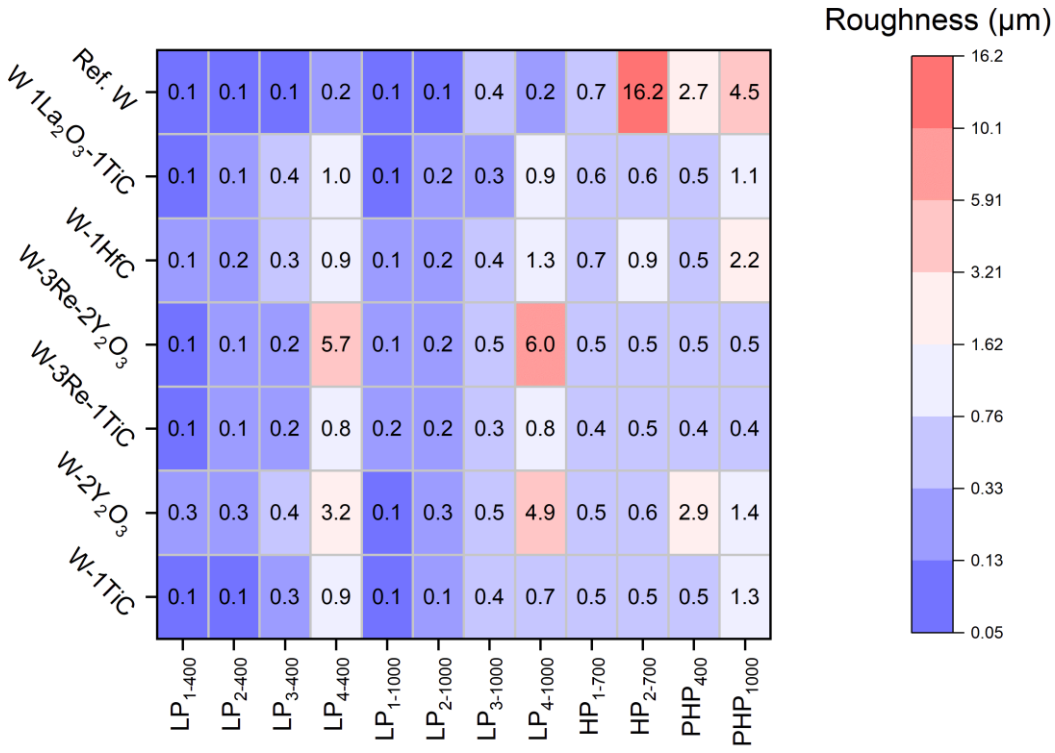


**Figure 4.** Heat map of the mean surface roughness ($R_a$) of every material tested under every condition, as shown in Table 2.

The tests with 100 pulses ($LP_1$ and $LP_2$) of all alloys showed no visible sign of surface modification or damage, even when inspected with an SEM. As shown in Table 1, W-2$Y_2O_3$ had worse behavior at both temperatures, with a significantly increased $R_a$. Other alloys behaved similarly to the reference tungsten at 400 °C, but their roughness slightly increased after $LP_{2\text{-}1000}$. After exposure to 1000 pulses with 0.38 GWm$^{-2}$ at 400 °C ($LP_{3\text{-}400}$), the trend continued, with all alloys increasing their roughness and the reference W showing no significant change. At 1000 °C ($LP_{3\text{-}1000}$), this difference could not be observed, with the reference W also showing increased roughness. The roughness increased the most for both samples containing yttria.

SEM images of all $LP_{3\text{-}1000}$ results are shown in Figure 5. The circular area affected by the laser can be identified by the rougher-looking surface. Despite their higher roughness, the yttria-containing samples showed no evidence of cracking, whereas all other alloys formed small, isolated cracks.

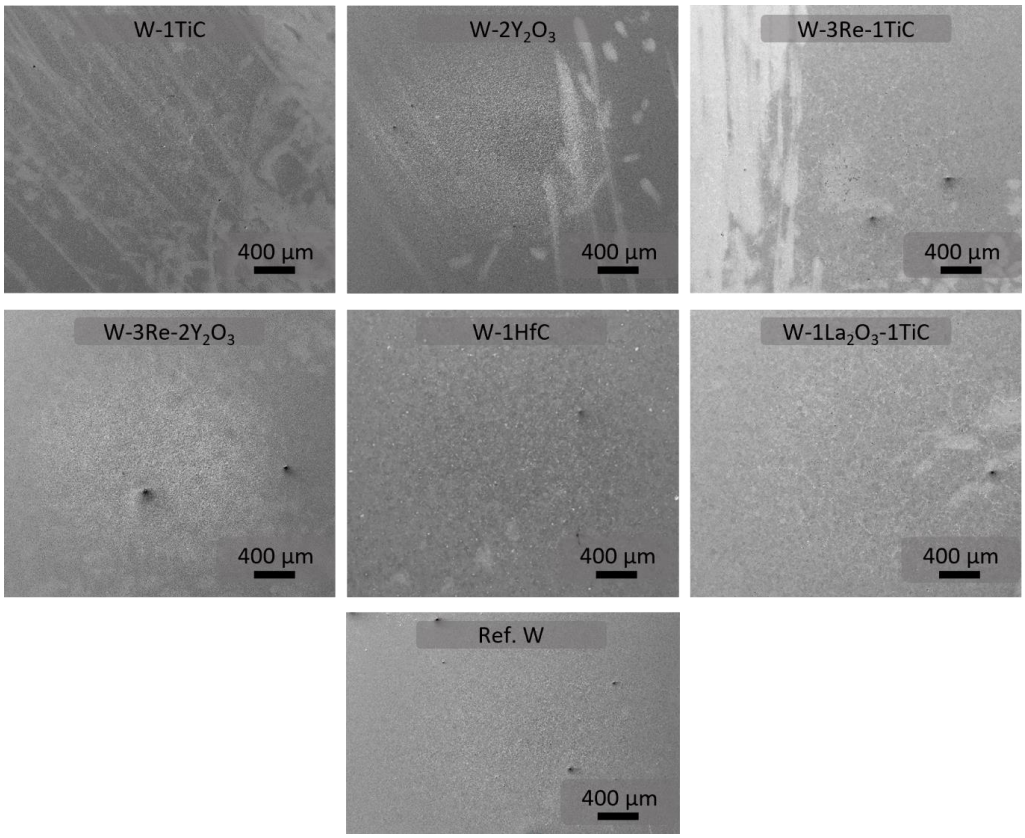


**Figure 5.** SEM micrographs of the samples tested at 1000 °C with 1000 laser pulses of 0.38 GWm$^{-2}$ ($LP_{3\text{-}1000}$).

The reference tungsten also showed a higher resistance to the high-power pulse ($LP_4$) at both temperatures, showing no signs of melting or damage and only a slightly higher surface roughness. The yttria-containing samples again showed a significantly higher roughness. Additionally, they showed large amounts of melting and some droplet ejection, which can be seen in Figure 6. This is to be expected, as $Y_2O_3$ has a melting point over 1000 °C lower than that of tungsten (2410 °C versus 3422 °C) and a lower thermal conductivity (27 versus 175 Wm$^{-1}$K$^{-1}$). $La_2O_3$ has an even lower melting point (2217 °C), but it was present in a lower amount than for the yttria-containing samples. The behavior of W-2$Y_2O_3$ and W-1TiC was similar to that observed for the disruption-like loads in Ref. [40].

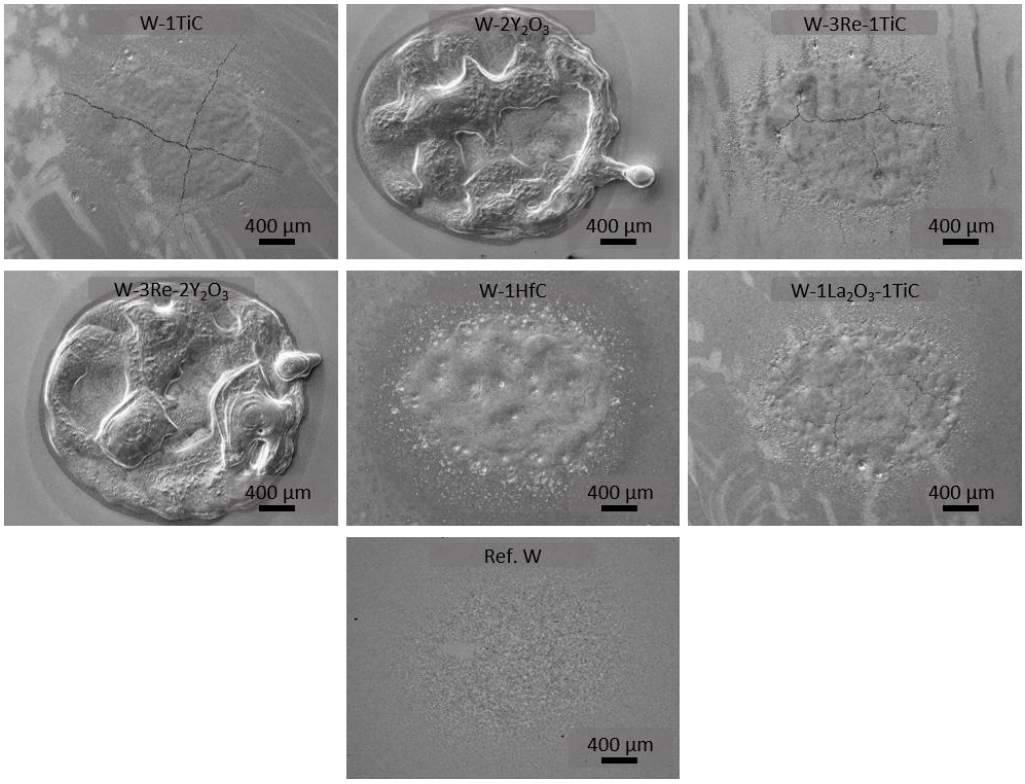


**Figure 6.** SEM micrographs of the samples tested at 1000 °C with 1 laser pulse of 1.6 $GWm^{-2}$ ($LP_{4\text{-}1000}$).

All other PIM samples also showed signs of melting in Figure 6, as well as signs of cracking in both samples containing TiC. Small craters were also seen on the sample surface, particularly for W-1HfC. This is a sign of the temperature reaching the boiling point of the materials, causing part of it to evaporate under the surface. This caused a pressure increase until the gas burst out, causing the observed damage.

The samples were then tested under a higher pulse number, namely $10^4$ ($HP_1$) and $10^5$ ($HP_2$), with an absorbed power density of 0.4 $GWm^{-2}$. This helps in understanding the behavior of the material under thermal shock fatigue throughout its lifetime due to the effect of ELMs. After $10^4$ pulses, all samples behaved similarly, with no evident damage and some surface roughening. However, after exposure to $10^5$ pulses, differences were more significant. The reference tungsten showed a large crack network (see Figure 7), with broad cracks and a much higher surface roughness (16.2 µm).

On the other hand, all PIM-W samples seemed to have tolerated the thermal shocks much better, with crack networks forming in the yttria-containing samples, but the cracks themselves were much thinner than those in the pure W (see Figure 7). W-1TiC also formed a crack network of thin cracks. In all cases, the surface roughness stayed low (<0.6 µm), except for W-1HfC, which had a slightly higher roughness (0.91 µm). The addition of TiC seemed to provide some resistance to damage from higher pulse numbers, as both W-3Re-1TiC and W-1$La_2O_3$-1TiC formed no cracks whatsoever, and W-1TiC only formed thin cracks. The more pronounced cracking of samples containing yttria seems to confirm their higher brittleness when compared with other materials, as demonstrated in [32,36].

To further understand the behavior of tungsten alloys when compared with ITER-grade tungsten, simultaneous exposure of the samples to plasma and thermal shocks was performed in the PSI-2 as described previously both at 400 °C (see Figure 8) and at 1000 °C (see Figure 9).

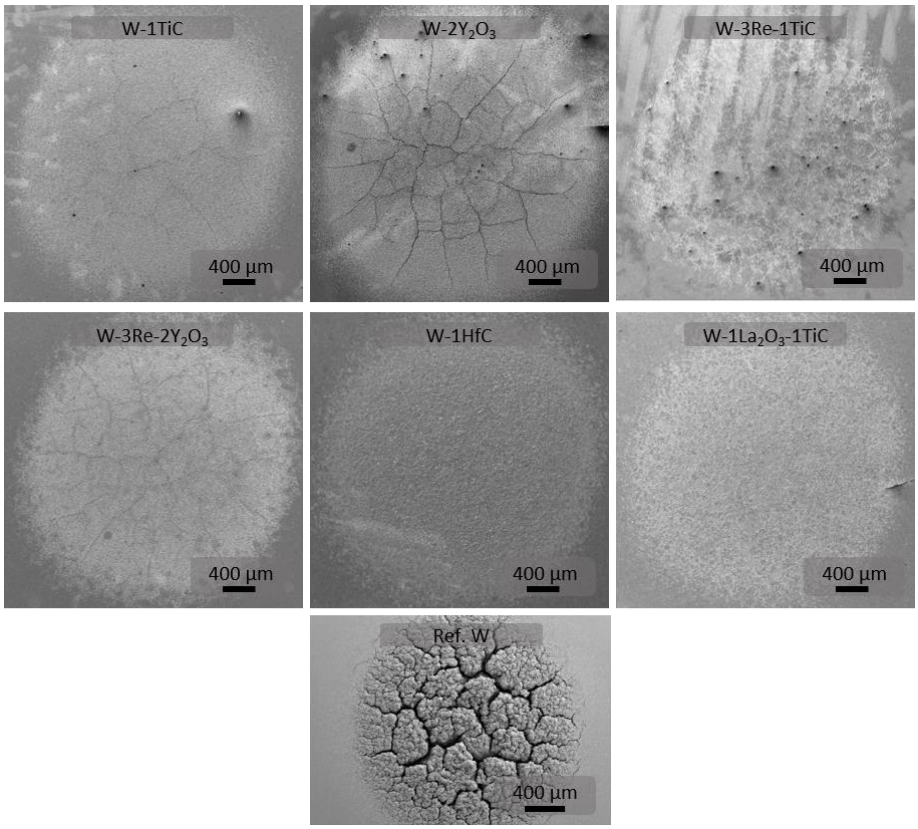


**Figure 7.** SEM micrographs of the samples tested at 700 °C with $10^5$ laser pulses of 0.4 $GWm^{-2}$ ($HP_{1\text{-}700}$).

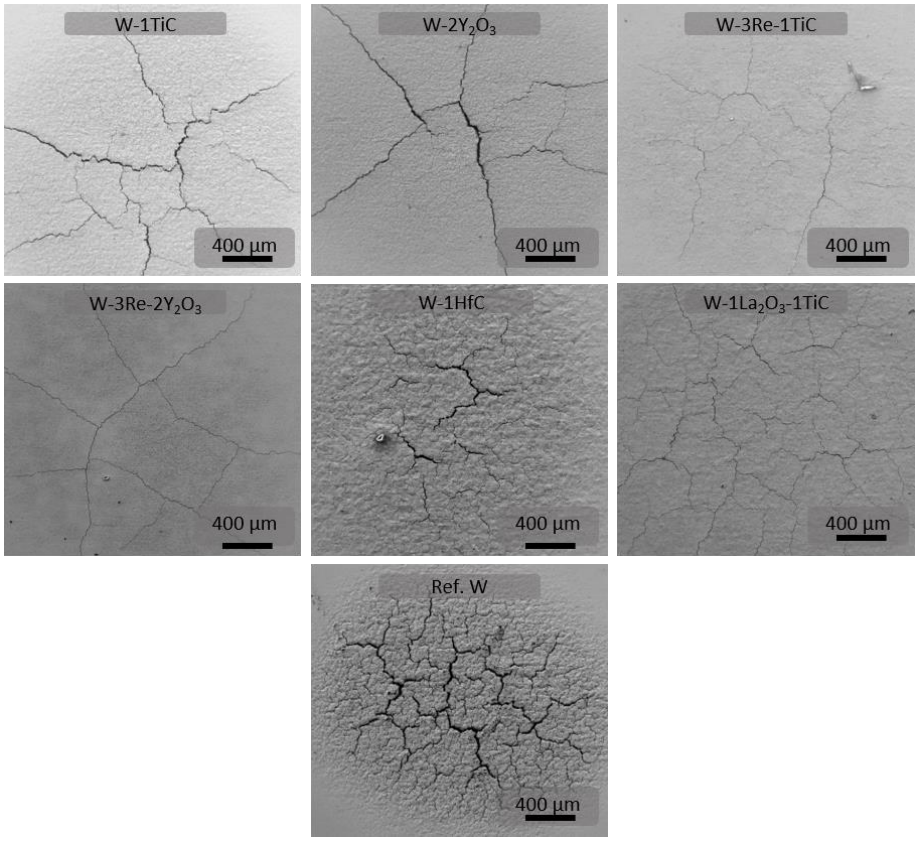


**Figure 8.** SEM micrographs of the samples tested at 400 °C with $10^5$ laser pulses of 0.4 $GWm^{-2}$ and a simultaneous total plasma fluence of $5 \times 10^{25}$ $m^{-2}$ of D/He (6%) plasma ($PHP_{400}$).

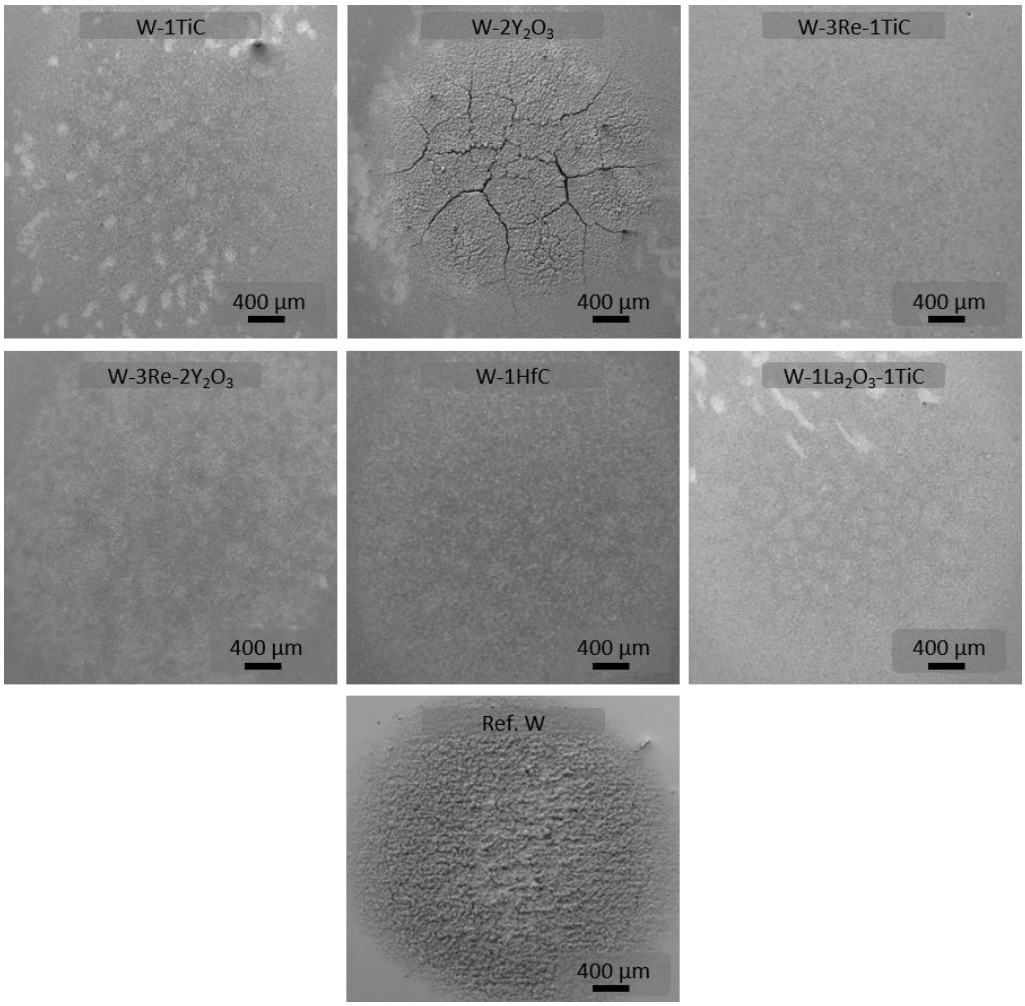


**Figure 9.** SEM micrographs of the samples tested at 1000 °C with $10^5$ laser pulses of 0.4 $GWm^{-2}$ and a simultaneous total plasma fluence of $5 \times 10^{25}$ $m^{-2}$ of D/He (6%) plasma ($PHP_{1000}$).

At 400 °C, all materials showed the formation of a crack network, while only W-2$Y_2O_3$ formed cracks during the tests at 1000 °C. This is a clear sign of how the operational temperature of a material or component can affect its performance. In this case, it is clear that none of the materials showed enough ductile behavior to prevent cracking at 400 °C. Even if they did show a lower DBTT than standard tungsten (as shown above in Figure 7 at 700 °C), the improvement was not enough at this operational temperature. The question of whether the DBTT can be further lowered by decreasing the grain size remains, as has been shown with fine-grained W-0.5ZrC, for example [41].

The temperature of 1000 °C is significantly higher than the DBTT of standard tungsten, which has a DBTT of about 600 °C [42]. By comparing the results of the tests with simultaneous plasma and heat loads at 400 °C and 1000 °C, it is clear that the damage observed in most cases was indeed lower for samples exposed at a higher temperature, mainly due to their improved ductility. For PHP1000, only W-2$Y_2O_3$ formed cracks, and most samples showed an increase in surface roughness. The rhenium-containing samples, W-3Re-1TiC and W-3Re-2$Y_2O_3$, had only a slight increase in roughness ($R_a$ = 0.4–0.5 µm). This indicates that using rhenium as an alloying element could increase its resistance to cracking thanks to the formation of a solid solution, which increases its strength and ductility (known as the "rhenium effect", which occurs in many BCC metals) [26]. However, the addition of yttria seemed to partially counteract this effect (see Figure 7), as the inclusion of $Y_2O_3$ can reduce the ductility of tungsten [32,36].

In most cases, there was no noticeable difference in the microstructural change of the different tungsten alloys after exposure to thermal shocks and plasma, with the only difference observed being the amount of damage and change in roughness. In some cases, however, such as those observed in Figure 10, second phases could be observed. In the yttria-containing alloys, particularly W-3Re-2$Y_2O_3$, darker, smaller grains were observed in the SEM images. Since some were also observed in W-2$Y_2O_3$, it can be assumed that these are yttria-rich grains. The darker color indicates a lower atomic mass in the SEM images, suggesting a high presence of yttria. These second phases were observed in the as-received samples as well (Figure 11, right) but with more regular, rounded shapes, as opposed to the elongated and irregular shapes observed after exposure in the PSI-2. The TiC-containing alloys also had a clear second phase, which could be identified as smaller, porous grains. In the as-received samples, they seemed to be smaller, as can be seen in Figure 11. After exposure, they seemed to have either coalesced and increased in size or appeared larger due to their surface being more exposed.

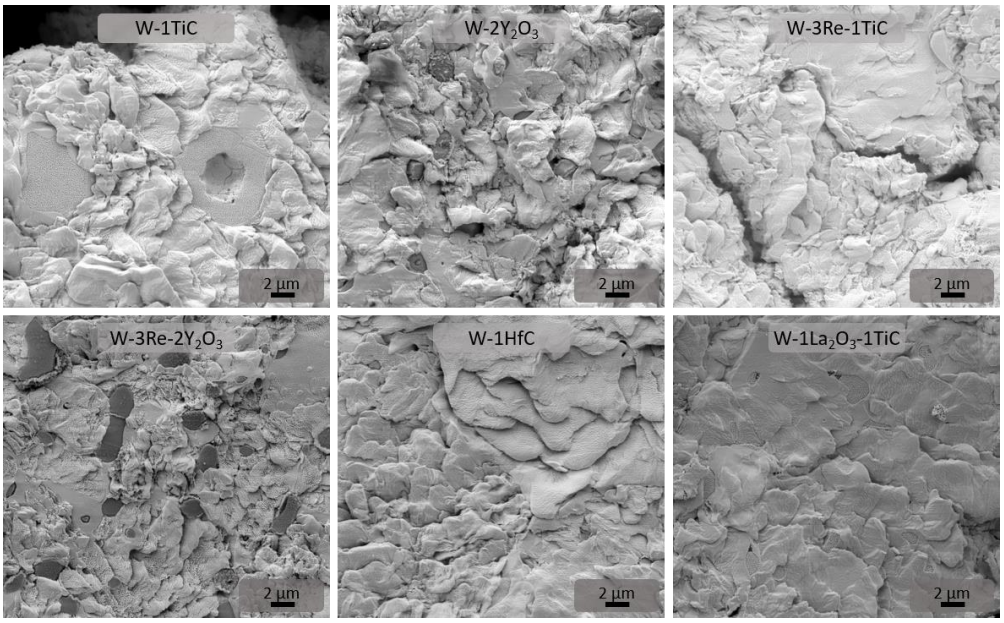


**Figure 10.** SEM micrographs showing the microstructural changes in the samples tested at 400 °C with $10^5$ laser pulses of 0.4 $GWm^{-2}$ and a simultaneous total plasma fluence of $5 \times 10^{25}$ $m^{-2}$ of D/He (6%) plasma ($PHP_{400}$).

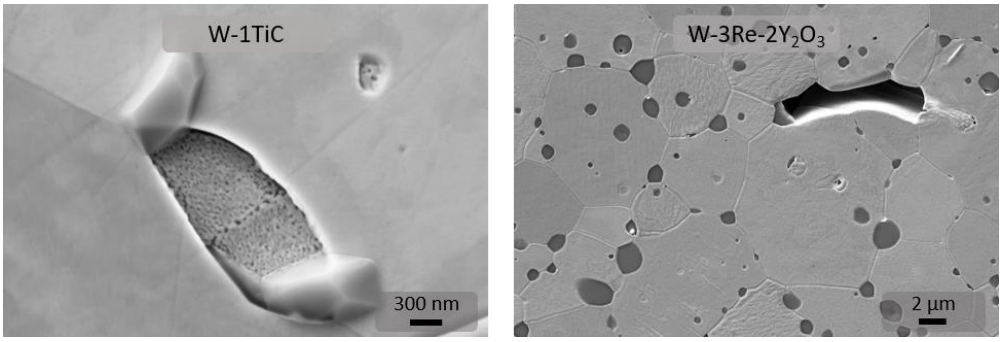


**Figure 11.** SEM micrographs showing the as-received microstructure of PIM-produced W-1TiC and W-3Re-2$Y_2O_3$.

## 4. Conclusions

Powder injection molding (PIM) allows the production of nearly net-shaped samples of different tungsten-based alloys. The performances of six tungsten-based alloys were compared (W-1TiC, W-2$Y_2O_3$, W-3Re-1TiC, W-3Re-2$Y_2O_3$, W-1HfC and W-1$La_2O_3$-1TiC) to the performance of ITER-grade tungsten under several different thermal shock and thermal shock with simultaneous plasma loading regimes (see Tables 1 and 2).

All materials had good behavior for the lower pulse number tests ($\leq$1000 pulses), although the standard tungsten performed slightly better, with no observable difference in surface roughness.

After the high-power shots, with one laser pulse of 1.6 $GWm^{-2}$ ($LP_{4\text{-}1000}$), the samples containing yttria showed evidence of melting and droplet ejection, the tungsten reference samples showed almost no change in surface roughness, and all other PIM samples had slightly elevated surface roughness values and evidence of surface melting. The samples containing TiC formed some cracks, while these could not be observed on W-HfC.

The high pulse number tests, with and without plasma, all showed the opposite trend of the lower pulse number tests. Here, the reference tungsten showed the most cracking and highest surface roughness of all materials, while the PIM-W alloys seemed to have a higher resistance to cracking. This can be attributed to the higher ductility of these alloys, particularly those containing rhenium. This means that tungsten-based alloys, whether produced via PIM or other methods, could potentially be used in certain areas of a fusion reactor. This can be particularly beneficial in those areas where the operation temperature will be lower than the DBTT of standard tungsten.

**Author Contributions:** Conceptualization, M.G. and M.W.; data curation, M.G.; formal analysis, M.G.; funding acquisition, C.L., B.U. and M.W.; investigation, M.G.; methodology, M.G. and M.W.; project administration, C.L., B.U. and M.W.; resources, S.A., A.K. (Alexander Klein), A.K. (Arkadi Kreter), C.L., M.R., B.U. and M.W.; software, M.G. and A.K. (Arkadi Kreter); supervision, B.U. and M.W.; visualization, M.G. and S.A.; writing—original draft, M.G.; writing—review and editing, M.G., S.A. and M.W. All authors have read and agreed to the published version of the manuscript.

**Funding:** This work was carried out within the framework of the EUROfusion Consortium, funded by the European Union via the Euratom Research and Training Programme (Grant Agreement No. 101052200—EUROfusion). The views and opinions expressed are, however, those of the author(s) only and do not necessarily reflect those of the European Union or the European Commission. Neither the European Union nor the European Commission can be held responsible for them.

**Data Availability Statement:** The data presented in this study are available on request from the corresponding author.

**Conflicts of Interest:** The authors declare no conflicts of interest.

## References

1. Hirai, T.; Escourbiac, F.; Carpentier-Chouchana, S.; Fedosov, A.; Ferrand, L.; Jokinen, T.; Komarov, V.; Kukushkin, A.; Merola, M.; Mitteau, R.; et al. ITER tungsten divertor design development and qualification program. *Fusion Eng. Des.* **2013**, *88*, 1798–1801. [CrossRef]
2. Pitts, R.; Carpentier, S.; Escourbiac, F.; Hirai, T.; Komarov, V.; Lisgo, S.; Kukushkin, A.; Loarte, A.; Merola, M.; Naik, A.S.; et al. A full tungsten divertor for ITER: Physics issues and design status. *J. Nucl. Mater.* **2013**, *438*, S48–S56. [CrossRef]
3. Pitts, R.; Bonnin, X.; Escourbiac, F.; Frerichs, H.; Gunn, J.; Hirai, T.; Kukushkin, A.; Kaveeva, E.; Miller, M.; Moulton, D.; et al. Physics basis for the first ITER tungsten divertor. *Nucl. Mater. Energy* **2019**, *20*, 100696. [CrossRef]
4. Federici, G.; Biel, W.; Gilbert, M.; Kemp, R.; Taylor, N.; Wenninger, R. European DEMO design strategy and consequences for materials. *Nucl. Fusion* **2017**, *57*, 092002. [CrossRef]
5. Gunn, J.; Carpentier-Chouchana, S.; Escourbiac, F.; Hirai, T.; Panayotis, S.; Pitts, R.; Corre, Y.; Dejarnac, R.; Firdaouss, M.; Kočan, M.; et al. Surface heat loads on the ITER divertor vertical targets. *Nucl. Fusion* **2017**, *57*, 046025. [CrossRef]

6. Linke, J.; Loewenhoff, T.; Massaut, V.; Pintsuk, G.; Ritz, G.; Rödig, M.; Schmidt, A.; Thomser, C.; Uytdenhouwen, I.; Vasechko, V.; et al. Performance of different tungsten grades under transient thermal loads. *Nucl. Fusion* **2011**, *51*, 73017. [CrossRef]
7. Ueda, Y.; Schmid, K.; Balden, M.; Coenen, J.; Loewenhoff, T.; Ito, A.; Hasegawa, A.; Hardie, C.; Porton, M.; Gilbert, M. Baseline high heat flux and plasma facing materials for fusion. *Nucl. Fusion* **2017**, *57*, 092006. [CrossRef]
8. Pintsuk, G. Tungsten as a Plasma-Facing Material. In *Comprehensive Nuclear Materials*; Elsevier: Amsterdam, The Netherlands, 2012; pp. 551–581.
9. Philipps, V. Tungsten as material for plasma-facing components in fusion devices. *J. Nucl. Mater.* **2011**, *415*, S2–S9. [CrossRef]
10. Pintsuk, G.; Bobin-Vastra, I.; Constans, S.; Gavila, P.; Rödig, M.; Riccardi, B. Qualification and post-mortem characterization of tungsten mock-ups exposed to cyclic high heat flux loading. *Fusion Eng. Des.* **2013**, *88*, 1858–1861. [CrossRef]
11. Wirtz, M.; Linke, J.; Loewenhoff, T.; Pintsuk, G.; Uytdenhouwen, I. Transient heat load challenges for plasma-facing materials during long-term operation. *Nucl. Mater. Energy* **2017**, *12*, 148–155. [CrossRef]
12. Gago, M.; Kreter, A.; Unterberg, B.; Wirtz, M. Synergistic effects of particle and transient heat loads on ITER-grade tungsten. *Phys. Scr.* **2020**, *T171*, 014007. [CrossRef]
13. Gago, M.; Kreter, A.; Unterberg, B.; Wirtz, M. Synergistic and separate effects of plasma and transient heat loads on the microstructure and physical properties of ITER-grade tungsten. *Phys. Scr.* **2021**, *96*, 124052. [CrossRef]
14. Gago, M.; Kreter, A.; Unterberg, B.; Wirtz, M. Bubble Formation in ITER-Grade Tungsten after Exposure to Stationary D/He Plasma and ELM-like Thermal Shocks. *J. Nucl. Eng.* **2023**, *4*, 204–212. [CrossRef]
15. Morgan, T.W.; Balden, M.; Schwarz-Selinger, T.; Li, Y.; Loewenhoff, T.H.; Wirtz, M.; Brezinsek, S.; De Temmerman, G. ITER monoblock performance under lifetime loading conditions in Magnum-PSI. *Phys. Scr.* **2020**, *T171*, 014065. [CrossRef]
16. Wirtz, M.; Kreter, A.; Linke, J.; Loewenhoff, T.; Pintsuk, G.; Sergienko, G.; Steudel, I.; Unterberg, B.; Wessel, E. High pulse number thermal shock tests on tungsten with steady state particle background. *Phys. Scr.* **2017**, *T170*, 014066. [CrossRef]
17. Brezinsek, S.; Coenen, J.; Schwarz-Selinger, T.; Schmid, K.; Kirschner, A.; Hakola, A.; Tabares, F.; van der Meiden, H.; Mayoral, M.-L.; Reinhart, M.; et al. Plasma–wall interaction studies within the EUROfusion consortium: Progress on plasma-facing components development and qualification. *Nucl. Fusion* **2017**, *57*, 116041. [CrossRef]
18. Baldwin, M.; Doerner, R. Formation of helium induced nanostructure 'fuzz' on various tungsten grades. *J. Nucl. Mater.* **2010**, *404*, 165–173. [CrossRef]
19. Kajita, S.; Yoshida, N.; Ohno, N. Tungsten fuzz: Deposition effects and influence to fusion devices. *Nucl. Mater. Energy* **2020**, *25*, 100828. [CrossRef]
20. Kajita, S.; Yoshida, N.; Ohno, N.; Tsuji, Y. Growth of multifractal tungsten nanostructure by He bubble induced directional swelling. *New J. Phys.* **2015**, *17*, 43038. [CrossRef]
21. Yao, G.; Shen, X.; Liu, J.-Q.; Zhu, X.-Y.; Luo, L.; Wu, Y. Study on damage behavior of the outer horizontal target in the EAST lower divertor after plasma operations. *Nucl. Mater. Energy* **2024**, *39*, 101640. [CrossRef]
22. Mutoh, Y.; Ichikawa, K.; Nagata, K.; Takeuchi, M. Effect of rhenium addition on fracture toughness of tungsten at elevated temperatures. *J. Mater. Sci.* **1995**, *30*, 770–775. [CrossRef]
23. Wurster, S.; Baluc, N.; Battabyal, M.; Crosby, T.; Du, J.; García-Rosales, C.; Hasegawa, A.; Hoffmann, A.; Kimura, A.; Kurishita, H.; et al. Recent progress in R&D on tungsten alloys for divertor structural and plasma facing materials. *J. Nucl. Mater.* **2013**, *442*, S181–S189. [CrossRef]
24. Stephens, J.R. Dislocation structures in single-crystal tungsten and tungsten alloys. *Met. Trans.* **1970**, *1*, 1293–1301. [CrossRef]
25. Garfinkle, M. Room-Temperature Tensile Behavior of 100 Oriented Tungsten Single Crystals with Rhenium in Dilute Solid Solution, NASA. Available online: https://ntrs.nasa.gov/api/citations/19660004949/downloads/19660004949.pdf (accessed on 20 June 2025).
26. Ren, C.; Fang, Z.; Koopman, M.; Butler, B.; Paramore, J.; Middlemas, S. Methods for improving ductility of tungsten—A review. *Int. J. Refract. Met. Hard Mater.* **2018**, *75*, 170–183. [CrossRef]
27. Lang, S.; Yan, Q.; Sun, N.; Zhang, X.; Deng, L.; Wang, Y.; Ge, C. Microstructure, basic thermal–mechanical and Charpy impact properties of W-0.1 wt.% TiC alloy via chemical method. *J. Alloys Compd.* **2016**, *660*, 184–192. [CrossRef]
28. Mabuchi, M.; Okamoto, K.; Saito, N.; Asahina, T.; Igarashi, T. Deformation behavior and strengthening mechanisms at intermediate temperatures in W-La2O. *Mater. Sci. Eng. A* **1997**, *237*, 241–249. [CrossRef]
29. Chen, P.; Xu, X.; Wei, B.; Chen, J.; Qin, Y.; Cheng, J. Enhanced mechanical properties and interface structure characterization of W–La2O3 alloy designed by an innovative combustion-based approach. *Nucl. Eng. Technol.* **2021**, *53*, 1593–1601. [CrossRef]
30. Nogami, S.; Hasegawa, A.; Fukuda, M.; Rieth, M.; Reiser, J.; Pintsuk, G. Mechanical properties of tungsten: Recent research on modified tungsten materials in Japan. *J. Nucl. Mater.* **2021**, *543*, 152506. [CrossRef]
31. Liu, R.; Zhou, Y.; Hao, T.; Zhang, T.; Wang, X.; Liu, C.; Fang, Q. Microwave synthesis and properties of fine-grained oxides dispersion strengthened tungsten. *J. Nucl. Mater.* **2012**, *424*, 171–175. [CrossRef]

32. Duerrschnabel, M.; Antusch, S.; Holtermann, B.; Jaentsch, U.; Baumgaertner, S.; Bonnekoh, C.; Hoffmann, M.; Hoffmann, J.; Rieth, M. Elucidating the microstructure of tungsten composite materials produced by powder injection molding. *Nucl. Mater. Energy* **2020**, *24*, 100766. [CrossRef]
33. Song, G.-M.; Wang, Y.-J.; Zhou, Y. Thermomechanical properties of TiC particle-reinforced tungsten composites for high temperature applications. *Int. J. Refract. Met. Hard Mater.* **2003**, *21*, 1–12. [CrossRef]
34. Antusch, S.; Norajitra, P.; Piotter, V.; Ritzhaupt-Kleissl, H.-J.; Spatafora, L. Powder Injection Molding—An innovative manufacturing method for He-cooled DEMO divertor components. *Fusion Eng. Des.* **2011**, *86*, 1575–1578. [CrossRef]
35. Antusch, S.; Commin, L.; Mueller, M.; Piotter, V.; Weingaertner, T. Two component tungsten powder injection molding—An effective mass production process. *J. Nucl. Mater.* **2014**, *447*, 314–317. [CrossRef]
36. Antusch, S.; Armstrong, D.E.; Ben Britton, T.; Commin, L.; Gibson, J.S.-L.; Greuner, H.; Hoffmann, J.; Knabl, W.; Pintsuk, G.; Rieth, M.; et al. Mechanical and microstructural investigations of tungsten and doped tungsten materials produced via powder injection molding. *Nucl. Mater. Energy* **2015**, *3–4*, 22–31. [CrossRef]
37. Loewenhoff, T.; Antusch, S.; Pintsuk, G.; Rieth, M.; Wirtz, M. High pulse number thermal shock testing of tungsten alloys produced by powder injection molding. *Nucl. Mater. Energy* **2019**, *20*, 100680. [CrossRef]
38. Kreter, A.; Brandt, C.; Huber, A.; Kraus, S.; Möller, S.; Reinhart, M.; Schweer, B.; Sergienko, G.; Unterberg, B. Linear Plasma Device PSI-2 for Plasma-Material Interaction Studies. *Fusion Sci. Technol.* **2015**, *68*, 8–14. [CrossRef]
39. Reiter, D.; Wolf, G.; Kever, H. Burn condition, helium particle confinement and exhaust efficiency. *Nucl. Fusion* **1990**, *30*, 2141–2155. [CrossRef]
40. Pintsuk, G.; Antusch, S.; Rieth, M.; Wirtz, M. Manufacturing and characterization of PIM-W materials as plasma facing materials. *Phys. Scr.* **2016**, *T167*, 14056. [CrossRef]
41. Yin, C.; Terentyev, D.; Pardoen, T.; Bakaeva, A.; Petrov, R.; Antusch, S.; Rieth, M.; Vilémová, M.; Matějíček, J.; Zhang, T. Tensile properties of baseline and advanced tungsten grades for fusion applications. *Int. J. Refract. Met. Hard Mater.* **2018**, *75*, 153–162. [CrossRef]
42. Davis, J.; Barabash, V.; Makhankov, A.; Plöchl, L.; Slattery, K. Assessment of tungsten for use in the ITER plasma facing components. *J. Nucl. Mater.* **1998**, *258–263*, 308–312. [CrossRef]